ACS OMEGA

http://pubs.acs.org/journal/acsodf

Article

Redox Activity of Noninnocent 2,2′-Bipyridine in Zinc Complexes: An Experimental and Theoretical Study

Bin Li, Blaise L. Geoghegan, Christoph Wölper, George E. Cutsail III,* and Stephan Schulz*

Cite This: *ACS Omega* 2021, 6, 18325−18332

Read Online

ACCESS | Metrics & More | Article Recommendations | Supporting Information

ABSTRACT: We report on a systematical reactivity study of β-diketiminate zinc complexes with redox-active 2,2′-bipyridine (bpy). The reaction of LZnI (L = HC[C(Me)N(2,6-*i*Pr$_2$C$_6$H$_3$)]$_2$) with NaB(C$_6$F$_5$)$_4$ in the presence of bpy yielded [LZn(bpy)][B(C$_6$F$_5$)$_4$] (**1**), with bpy serving as a neutral ligand, whereas reduction reactions of LZnI with 1 or 2 equiv of KC$_8$ in the presence of bpy gave the radical complex LZn(bpy) (**2**) and [2.2.2-Cryptand-K][LZn(bpy)] (**3**), in which bpy either acts as a π-radical anion or a diamagnetic dianion, respectively. The paramagnetic nature of **2** was confirmed via solution magnetic susceptibility measurements, and UV−vis spectroscopy shows that **2** exhibits absorption bands typical for bpy radical species. The EPR spectra of **2** and its deuterated analog **2-*d*$_8$** demonstrate that the spin density is localized to the bpy ligand. Density functional theoretical calculations and natural bond orbital analysis were employed to elucidate the electronic structure of complexes **1**−**3** and accurately reproduced the structural experimental data. It is shown that reduction of the bpy moiety results in a decrease in the β-diketiminate co-ligand bite angle and elongation of the Zn−N(β-diketiminate) bonds, which act cooperatively and in synergy with the bpy ligand by decreasing Zn−N(bpy) bond lengths to stabilize the energy of the LUMO.

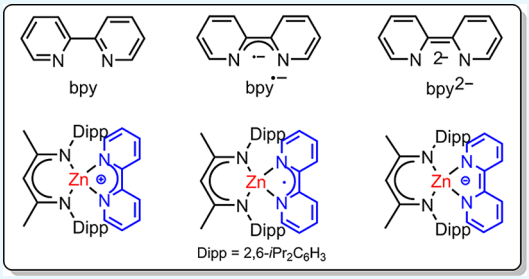

INTRODUCTION

The redox-active bidentate ligand 2,2′-bipyridine (bpy) has been extensively used in coordination chemistry,[1−3] supramolecular and macromolecular chemistry,[4−6] catalysis,[7−9] and photoelectrochemistry[10,11] due to its electronic flexibility. bpy can adopt three different oxidation states and serve as a neutral bpy ligand (bpy^0), a monoradical anion (bpy$^{\bullet-}$), and a diamagnetic dianion (bpy^{2-}) (Figure 1), and numerous main

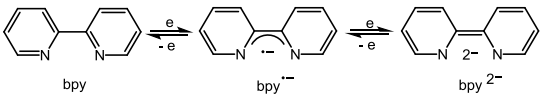

Figure 1. Variable oxidation levels of 2,2′-bipyridine.

group metal,[12−18] transition metal, and f-block metal[19,20] complexes have been reported. The stepwise reduction of neutral bpy^0 to the radical anion and dianion due to the population of the π* orbitals (LUMO) with one or two electrons not only affects the bonding metrics, i.e., a shortening of the bridging C−C bond is observed, but also influences the electronic properties of the bpy ligand. While both the neutral bpy^0 and the radical anion bpy$^{\bullet-}$ are good σ donors but weak π acceptors, the dianion bpy^{2-} is a strong π donor.[21,22] Due to the poor π-acceptor properties of bpy, electron-rich metals are unable to engage in π backbonding; thus, the bond metrics of the bpy moiety are directly related to the oxidation state of the bpy ligand. This allows for the identification of the specific oxidation level of bpy using single-crystal X-ray diffraction.[22] A strong correlation between the bonding metrics and the oxidation states of the bpy ligand was found by comparing experimental and calculated bond lengths within multiple series of metal complexes, i.e., [(Cp)$_2$*M*(bpy)]^n (*M* = V, *n* = 0, +, 2+; *M* = Ti, *n* = −, 0, +, 2+; *M* = Zr, *n* = 0), [(Cp*)$_2$Ti(bpy)]^0, [(Cp*)*M*(bpy)]^n (*M* = Co, *n* = 0, +; *M* = Ru, *n* = −; Cp* = C$_5$Me$_5$), [(Cp*)Co(bpy)Cl]^n (*n* = 0, +), and [Mn(CO)$_3$(bpy)]$^-$, showing that the bpy bonding regime is invariant to the type of coordinated metal.[22] Moreover, a series of group 6 and 7 metal complexes [*M*(bpy)$_3$]^n (*M* = Mn, Tc, Re; *n* = −, 0, +, 2+) and [Cr(^{t}bpy)$_3$]^n (*n* = 0, +, 2+, 3+; ^{t}bpy = 4,4′-*t*Bu$_2$-2,2′-bipyridine) in different oxidation states were studied using a combination of experimental techniques and density functional theoretical (DFT) calculations, showing a linear dependency between bonding metrics and overall charges.[23,24] Comparable findings were reported for first-row transition metal complexes [(mes)$_2$*M*(bpy)]^n (*M* = Cr, Mn, Fe, Co, Ni; *n* = 0, −; mes = 2,4,6-Me$_3$C$_6$H$_2$).[25,26]

Although the redox-active character of bpy has been demonstrated, there is still a high demand to produce further structurally well-characterized examples of metal complexes of

Received: April 26, 2021
Accepted: May 18, 2021
Published: July 6, 2021

the reduced bpy ligands to elucidate their electronic structures. Previously, both the radical anion $bpy^{\bullet-}$ and dianion bpy^{2-} species have been suggested to be π-donating ligands in metal complexes with vacant d orbitals (i.e., Cr, Ti, etc.) that may act as π acceptors.[21,22] Despite this possible π backdonation of the reduced bpy ligands, the ability to form bpy complexes with late-stage d-block metals such as Zn is well-known. However, in most cases, bpy acts simply as a neutral bpy^0 donor, and although investigations on heteroleptic complexes containing the $Zn(bpy^0)$ motif have been conducted, the electronic structures of such complexes with reduced bpy ligands $bpy^{\bullet-}$ and bpy^{2-} have, up until now, not been well-characterized.[27] Here, we provide extensive experimental and computational characterization of the neutral and reduced forms of the Zn−bpy motif ($Zn-bpy^0$, $Zn-bpy^{\bullet-}$, and $Zn-bpy^{2-}$) in a heteroleptic complex and elucidate their structural and electronic characteristics. The noninnocence of bpy is crystallographically and theoretically discussed, and a correlation between the variable oxidation states of bpy and the structural parameters is provided.

RESULTS AND DISCUSSION

β-Diketiminato ligands have been extensively used in the assembly of a wide variety of metal complexes in various oxidation states.[28,29] Although the oxidative redox noninnocence of the β-diketiminato ligand has been spectroscopically and theoretically identified,[30−32] the reductive redox behavior is limited to a specific ligand, $HC[C(Ph)N(SiMe_3)]_2$.[33] We, therefore, reacted LZnI (L = $HC[C(Me)N(2,6\text{-}iPr_2C_6H_3)]_2$) with $NaB(C_6F_5)_4$ in the presence of 2,2′-bipyridine, yielding $[LZn(bpy)][B(C_6F_5)_4]$ (**1**) (Scheme 1),

Scheme 1. Synthesis and Conversion of 1−3[a]

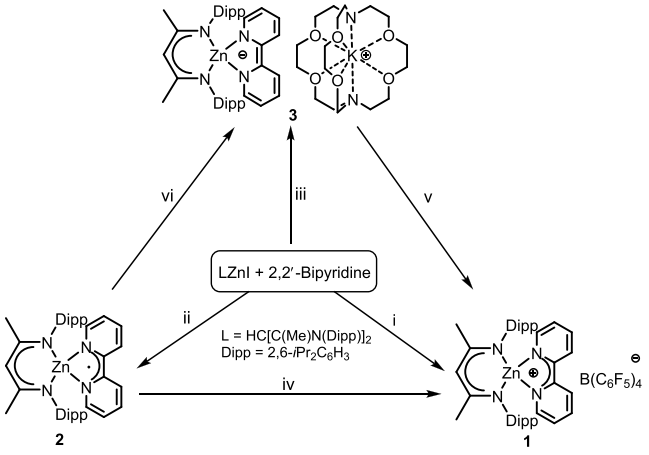

[a]Reagents and condition: (i) $NaB(C_6F_5)_4$, *n*-hexane; (ii) KC_8, toluene; (iii) 2 KC_8, [2.2.2]cryptand, THF; (iv) $[Ph_3C][B(C_6F_5)_4]$, CD_2Cl_2; (v) 2 $[Ph_3C][B(C_6F_5)_4]$, THF-d_8; and (vi) KC_8, [2.2.2]-cryptand, THF-d_8.

with 2,2′-bipyridine serving as a neutral (bpy^0) ligand. Compound **1** is soluble in polar solvents, i.e., THF, CH_2Cl_2, and fluorobenzene, but only slightly soluble in *n*-hexane and toluene. The ^{1}H NMR spectrum of **1** in CD_2Cl_2 shows the characteristic resonances of the β-diketiminate ligand, i.e., singlets at 1.85 and 5.15 ppm of the Me groups and the γ-C*H* proton, two doublets (0.72 and 1.18 ppm) and one septet (3.11 ppm) of the *i*Pr group, while resonances at 7.78, 8.22, and 8.61 ppm belong to bpy^0 (Figure S2).

To investigate the formation of different oxidation states of the bpy ligand, LZnI was reacted with 1 equiv of KC_8 in the presence of 1 equiv of bpy in toluene. Black crystals of **2** were isolated from the resulting black solution in a yield of 38.8% (Scheme 1). The ^{1}H NMR spectrum of **2** in THF-d_8 shows broad resonances typical of a paramagnetic species.[34] The paramagnetic character of **2** was confirmed by solution magnetic susceptibility measurements via the Evans method.[35] The room-temperature magnetic susceptibility of **2** was measured as 1.76 μ_B, indicating the presence of a single-unpaired electron, which is consistent with the single-crystal structure and electron paramagnetic resonance (EPR) spectroscopy (see below). Compound **2** is stable at ambient temperature under an inert gas atmosphere but thermally decomposes at 200 °C. As expected, the oxidation of **2** with $[Ph_3C][B(C_6F_5)_4]$ led to the quantitative formation of **1** (Figure S25).

The reaction of LZnI with 2 equiv of KC_8 in the presence of bpy and [2.2.2]cryptand in THF (Scheme 1) as well as the reduction of **2** with KC_8 in THF (Figure S27) yielded complex **3** as dark violet crystals. The ^{1}H NMR spectrum of **3** in THF-d_8 shows the resonances of the β-diketiminate ligand (δ 4.48 (γ-C*H*), 1.56 (Me), 1.16, 1.37, 3.47 ($CHMe_2$)) and the [2.2.2]cryptand (2.52, 3.51, and 3.55 ppm), whereas resonances of the bpy ligand could not be detected. Likewise, the ^{1}H NMR spectrum of **3** in CD_3CN shows the same phenomenon (Figure S23). In contrast, the ^{1}H NMR spectrum of **3** in CD_2Cl_2 shows the expected resonances of the β-diketiminate and bpy ligands as well as the [2.2.2]cryptand. The relative intensity of the resonances of the cation and anion deviates from the expected 1:1 ratio, which is probably due to the partial reoxidation of bpy^{2-} to bpy^0 caused by its reaction with CD_2Cl_2. This is further supported by various 2D NMR analyses of **1** and **3** in CD_2Cl_2 (Figures S4, S5, S21, and S22). The different ^{1}H NMR spectra of **3** in THF-d_8 and in CD_2Cl_2 indicate a dynamic behavior of **3** in these solvents. We, therefore, performed a variable temperature ^{1}H NMR analysis of **3** in THF-d_8 in the temperature range from −60 to +50 °C, but no change was observed except that the resonance of the [2.2.2]cryptand was displayed at 3.53 ppm at −60 °C (Figure S28). In addition, we reacted an isolated sample of **3** with $[Ph_3C][B(C_6F_5)_4]$ in a 1:2 molar ratio in THF. This reaction quantitatively yielded compound **1** (Figure S26), proving the presence of bpy in the solution of **3** in THF. Moreover, recrystallization experiments of **3** from solutions in toluene and *n*-hexane/THF gave the same molecular structures (Figures S31 and S32). The EPR spectrum of compound **3** in THF closely matches the relatively strong signal of compound **2** in THF (Figure S40), indicating partial oxidation of **3** to **2**. Because the UV−vis spectra of compounds **2** and **3** are also similar (see the UV−vis Spectra section), we conclude that compound **3** in THF at least partially forms complex **2** ($bpy^{\bullet-}$), and these residual quantities of **2** significantly influence the NMR resonances corresponding to the bpy moiety due to the fast electron exchange as well as contributing characteristic $\pi \rightarrow \pi^*$ absorption bands in the UV−vis spectrum.

Solid State Structures. The solid-state structures of **1**−**3** were determined by single-crystal X-ray diffraction. Compound **1** was recrystallized from *n*-hexane/fluorobenzene, and **2** was crystallized from toluene. Single crystals of compound **3** were

https://doi.org/10.1021/acsomega.1c02201
ACS Omega 2021, 6, 18325−18332

grown from toluene (**3**) and *n*-hexane/THF (**3#**). Since both structures are comparable, only the structural parameters of **3** are discussed. Compound **1** crystallizes in the monoclinic space group $P2_1/n$, while **2** and **3** crystallize in the triclinic space group $P\bar{1}$ (Figure 2). The zinc atoms in **1**−**3** adopt

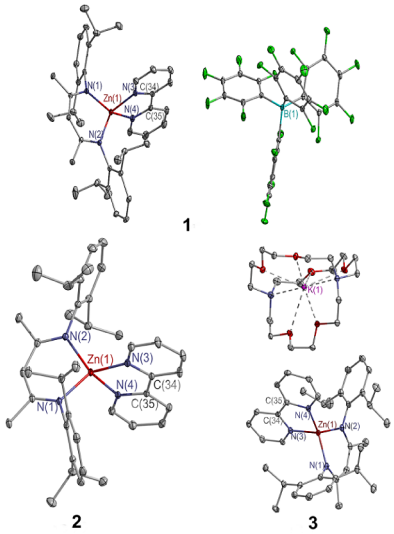

Figure 2. Molecular structures of **1** (top), **2** (bottom, left), and **3** (bottom, right) with thermal ellipsoids at the 30% probability level. H atoms and solvent molecules are omitted for clarity.

distorted tetrahedral coordination geometries. The plane defined by Zn, N1, and N2 is approximately perpendicular to the bipyridyl plane (88.99°, **1**; 89.34°, **2**; 88.29°, **3**). The C−C bond lengths in the bpy moiety clearly reflect the different charges of the bpy ligand, resulting from the stepwise population of the π^* orbitals of the bpy ligand. The bridging C34−C35 bond lengths decrease from 1.485(2) Å in **1** to 1.4269(16) Å in **2** and, finally, 1.384(4) Å in **3**, which agrees with previously described changes in the bpy bond lengths as a consequence of the reduction of the complex.[23−26] Moreover, in the five-membered Zn(bpy) chelate, the stepwise reduction results in an elongation of the neighboring C−N bonds from 1.348(2) Å in **1** to 1.384(14) Å in **2** and, finally, 1.430(4) Å in **3**, whereas a shortening of the Zn−N bond lengths from 2.064(14) Å in **1** to 1.997(10) Å in **2** and 1.958(3) Å in **3** is observed. As a result of the bond length variation, the N3−Zn−N4 angle of the bpy ligand increases stepwise from 80.11(6)° to 86.23(11)° in **1**−**3**, as was previously reported.[22−26] However, the Zn−N bond lengths within the β-diketiminate ligand steadily increase from 1.949(13) (**1**) over 1.977(10) (**2**) to 2.024(3) Å (**3**), while the N1−Zn−N2 bond angle of the β-diketiminate ligand steadily decreases from 100.70(5)° in **1** to 97.89(4)° in **2** and 94.82(11)° in **3**, respectively.

EPR of 2. The room-temperature Continuous Wave (CW) X-band (∼9.45 GHz) spectrum of **2** is centered near the free electron value g_e = 2.0023 and is approximately 30 G wide (Figure 3). The EPR spectrum of **2** has a large number of resolved hyperfine features and is similar to the previously reported alkylzinc-2,2′-bipyridyl (bpy) radical complex [(bpy)-Zn(Et)] (Et = ethyl),[36] suggesting that **2** possesses a similar localized radical bpy ligand with various ^{1}H hyperfine couplings.

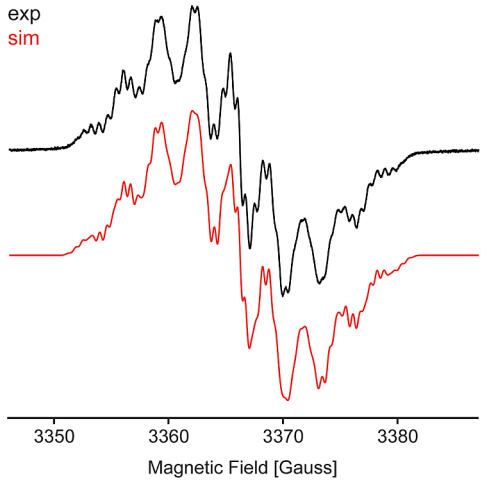

Figure 3. Experimental (black) and simulated (red) room-temperature solution X-band CW EPR spectra for **2**. Simulated parameters for **2**: g_{iso} = 2.00236, $a_{iso}(N,N'\{bpy\})$ = 9.08 MHz, $a_{iso}(H_{6,6'})$ = 1.62 MHz, $a_{iso}(H_{5,5'})$ = 9.83 MHz, $a_{iso}(H_{4,4'})$ = 5.92 MHz, $a_{iso}(H_{3,3'})$ = 2.57 MHz, and $a_{iso}(N,N'\{\beta\text{-diketiminate}\})$ = 1.62 MHz, line-width (peak-to-peak) = 0.54 gauss.

To experimentally confirm that the radical is localized to the bpy ligand and to refine the ^{14}N hyperfine couplings, the fully deuterated bpy analog (**2-*d*$_8$**) was prepared and measured via EPR (Figure S38). In **2-*d*$_8$**, the equivalent ^{2}H hyperfine couplings scale by the gyromagnetic ratio ∼1/6.5, yielding significantly diminished ^{2}H couplings compared to the ^{1}H couplings in **2**. **2-*d*$_8$** exhibits a five-line spectrum arising from 2 equiv ^{14}N(I = 1) nuclei, confirming that the radical is bpy centered. This, in turn, eliminates the possibility of large hyperfine contributions from the ^{14}N atoms of the β-diketiminate co-ligand to the EPR spectrum and allows for the further refinement of ^{1}H bpy hyperfine couplings.

Ultimately, the multiline spectrum of **2** can be accurately simulated using a complex hyperfine regime, whereby the magnitude of the isotropic ^{14}N and ^{1}H hyperfine interactions (a_{iso}) may be simulated in equivalent atomic pairs across the two pyridyl rings (Figure 1) and small additional hyperfine couplings from 2 equiv ^{14}N nuclei on the β-diketiminate co-ligand (a_{iso} ∼1.62 MHz). The a_{iso} values obtained from the simulated spectrum and DFT calculations for the radical complex **2** (Figure S39) are detailed in Table S2 alongside the calculated hyperfine couplings for the free bpy radical anion. The trends in the DFT calculated hyperfine couplings are in good agreement with the values obtained from the simulated spectrum, allowing for atomic assignments to be made, which are in agreement with those made previously.[31] DFT also calculates small ^{14}N hyperfine couplings for the two β-diketiminate ^{14}N nuclei ($N,N'\{\beta\text{-diketiminate}\}^{DFT}$ = 1.91 MHz), which is in agreement with the simulation of the experimental spectrum.

UV−Vis Spectra. The UV−vis absorption and associated time-dependent DFT-calculated spectra for complexes **1**−**3** are shown in Figures S34−S37. Complex **2** exhibits a characteristic intense $\pi \rightarrow \pi^*$ transition on the bpy$^{\bullet-}$ moiety at ∼26 100 cm^{-1} (ε = 2.24 × 10^4 M^{-1} cm^{-1}) and a less intense $\pi^* \rightarrow \pi^*$ transition at ∼19 500 cm^{-1} (0.59 × 10^4 M^{-1} cm^{-1}), which are in agreement with the values previously reported for [Na$^+$bpy$^{\bullet-}$ (THF)] and [Cr(CO)$_4$(bpy$^{\bullet-}$)].[37,38] In bpy^0, the $\pi \rightarrow \pi^*$ transition occurs at a much higher energy of 35 700

https://doi.org/10.1021/acsomega.1c02201
ACS Omega 2021, 6, 18325−18332

cm^{-1} as the π^* orbital is further destabilized when completely unpopulated.[37] However, in **1**, this absorption band is at a slightly lower energy of 31 700 cm^{-1}. **3** in THF exhibits a UV−vis spectrum with less intense absorption bands that are similar to those for **2**, suggesting that some $bpy^{\bullet-}$ species (**2**) are formed upon dissolution of **3** in THF (Figure S34B), as discussed above. Finally, **3** in CH_2Cl_2 yielded no measurable radical signal by EPR spectroscopy (Figure S40), in agreement with the absence of $bpy^{\bullet-}$ absorption features.

Quantum Chemical Calculations. Geometry-optimized structures of **1**−**3** are in excellent agreement with the experimental structures (Figure S41) and accurately reproduce the tetrahedral distortion of the ZnN_4 first coordination sphere of **1** upon reduction to **2** and then **3**. The optimized structures reproduce the shortening of the Zn−N(bpy) bond lengths upon reduction from an average of 2.063 Å in **1** to 2.003 Å in **2** and, finally, 1.958 Å in **3** (Table S3 and Figure 4). DFT also

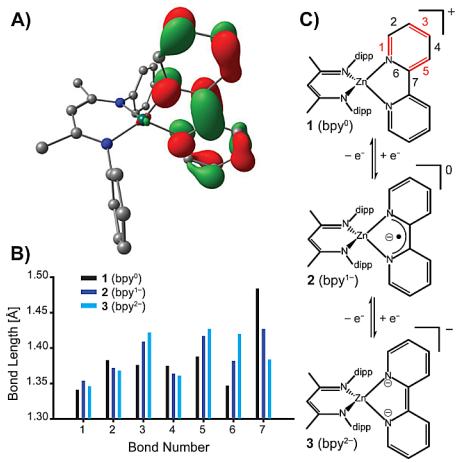

Figure 4. (a) B3LYP/def2-TZVP calculated SOMO in **2** (isopropyl groups and hydrogen atoms omitted for clarity). (b) Bond length changes across the bpy ligand in complexes **1**−**3**. (c) Schematic view of the Lewis structures of the neutral, radical anionic, and dianionic bpy ligands in **1**−**3**. Hydrogen atoms and isopropyl residues omitted for clarity.

captures the alterations to the N−C and C−C bond lengths and bond angles of the bpy fragment, which are expected due to the filling of bpy π^* orbitals upon reduction and the concomitant rearrangement of the π-bonding structure of the neutral ligand. This is generally characterized by a large decrease in the bridging C34−C35 bond length, calculated as 1.484 Å in **1** and decreasing to 1.428 and 1.401 Å in **2** and **3**, respectively (Figure 4b).[25]

DFT also reproduces the changes in bond metrics pertaining to the Zn−β-diketiminate fragment, which responds in opposing fashion to the Zn−bpy fragment. The mean of the two Zn−N(β-diketiminate) bond lengths of the DFT-optimized structures increases upon reduction of **1** from 1.981 Å to 2.015 Å in **2** and 2.051 Å in **3**. Second, there is an incremental decrease in the N−Zn−N angle of the Zn−β-diketiminate fragment from 101.68° to 94.94° in **1**−**3**, which along with the decrease in Zn−N(β-diketiminate) bond lengths are in line with the crystallographic data.

Crystallographic and computational analyses of R_2Zn complexes with N-donor co-ligands [e.g., Me_2Zn(bpy)] showed that a 10.0° decrease in the C−Zn−C bond angle can lead to Zn−N bond lengths shortening by up to 0.06 Å.[39] Between complexes **1** and **3**, the β-diketiminate N−Zn−N angle decreases by only 6.7°, but the bpy Zn−N bond lengths decrease by 0.07 Å, showing that the effects of angular distortion about the Zn atom on the Zn−N bonds of the co-ligand are not limited to dialkylzinc complexes but are also apparent in complexes with N_4 first-coordination spheres.

Considering there is a simultaneous reduction of the bpy ligand, the changes in the Zn−bpy bond metrics are not solely attributed to the angular distortions of the Zn−β-diketiminate motif but are also subject to the changes in the electronic structure of the bpy ligand. The single-point energies of **2** and **3** are calculated to be ca. 2.6 and 5.0 eV higher than **1**, respectively, showing a consistent energy increase with reduction. A comparison of the frontier molecular orbitals (MOs) shows that the cationic species **1** has a highest occupied molecular orbital (HOMO) with electron density distributed across the supporting β-diketiminate ligand (Figure 5). Meanwhile, the LUMO of **1** consists of an aromatic bpy

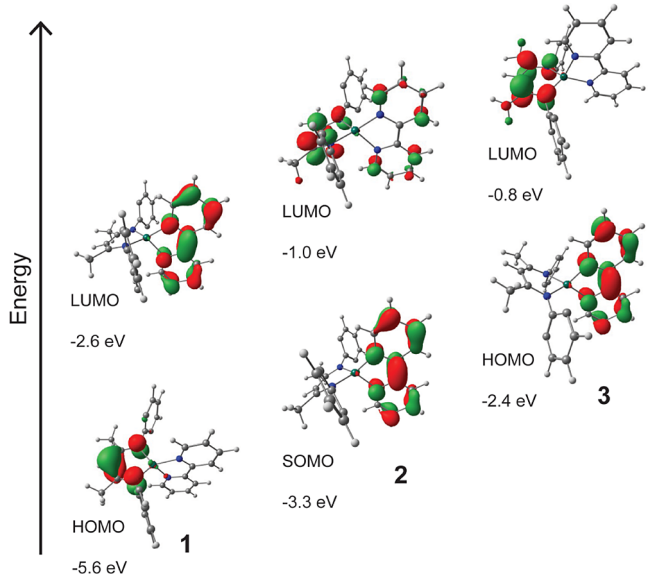

Figure 5. HOMO/SOMO and LUMO energies for **1**, **2**, and **3**. Isosurfaces are plotted with a value of 0.05. Certain isopropyl residues are omitted for clarity. Legend: zinc, blue-green; nitrogen, blue; carbon, gray; hydrogen, white.

moiety. In contrast to **1**, the SOMO of **2** and HOMO of **3** are MOs exhibiting electronic delocalization on the bpy, with noticeable nodes occurring on the C30 and C39 positions of the rings. The SOMO and corresponding spin density plot of **2** shown in Figure S42 make the magnitude and signs of the ^1H hyperfine couplings (Table S2) apparent, where the largest are at C31/C38 and C32/C37 and the weakest at the effective nodes of spin density at C30 and C39.

We have additionally performed natural bond analysis[40] (NBO) to formalize the localized orbitals that describe the molecular bonding pattern of electron pairs (or of individual electrons in the open-shell case) in an optimally compact form for complexes **1**−**3**. Bond hybridization, type (σ−σ^*/π−π^*), and polarization for each atom pair within the bpy fragments are given in Tables S4−S6. The natural charges (NCs) for each atom are obtained from the natural population analysis[41] (NPA) and are shown in Table 1. The natural electronic configuration of the Zn atom of complexes **1**−**3** are identical: $[Ar]4s^{0.33}\ 3d^{9.97}\ 4p^{0.02}\ 4d^{0.01}$ with 10.30 valence electrons, in

https://doi.org/10.1021/acsomega.1c02201
ACS Omega 2021, 6, 18325−18332

Table 1. Atomic Natural Charges from the Natural Population Analysis (α and β Spins Combined)

atom	charge		
	1	2	3
Zn1	1.664	1.666	1.667
N3	−0.586	−0.681	−0.785
N4	−0.589	−0.679	−0.804
C30	0.063	0.052	0.051
C31	−0.222	−0.313	−0.430
C32	−0.131	−0.193	−0.261
C33	−0.201	−0.215	−0.249
C34	0.164	0.096	0.027
C35	0.170	0.097	−0.004
C36	−0.197	−0.211	−0.243
C37	−0.125	−0.191	−0.284
C38	−0.223	−0.308	−0.439
C39	0.062	0.054	0.037
N1	−0.78	−0.750	−0.73
N2	−0.78	−0.748	−0.73

line with the previously reported Zn-radical species.[42] The NPA shows that the NC on the Zn atoms remains consistently at a value near +1.66 (Table 1), confirming that the reduction of **1** does not influence the local electronic structure of the Zn(II) ions. Similarly, the coordinating N atoms of the supporting β-diketiminate ligand do not exhibit significant changes in their NCs, remaining redox innocent. Conversely, the NC decreases significantly on both of the bpy nitrogen atoms as the complexes are reduced. There is a uniform decrease in the NCs across all other atoms on the bpy fragment; the consequence of singly and then doubly populating the π^* orbital in **2** and then **3**, respectively. This shows that both electrons reside within the same MO on the dianionic bpy ligand, in agreement with the DFT-calculated HOMOs (Figure 5). Ultimately, the analysis of the NCs for **1**−**3** concludes that a reduction of **1** and **2** is localized to the bpy.

The formal d^{10} Zn center is unable to partake in π-backbonding between the Zn d-manifold and the bpy π^* orbitals, limiting the Zn−bpy and Zn−β-diketiminate interactions to σ-type interactions and electrostatic forces only. This effect has also been reported in a range of heteroleptic first-row transition metal complexes of bpy.[24,25]

The frontier orbitals exhibit solely ligand character and Zn *d* character is absent, demonstrating how low the Zn *d* manifold is in energy relative to the valence ligand orbitals—similar to other pyridine- and pyrrole-coordinated Zn(II) complexes.[43] Thus, based on the structural evidence, the interactions between the Zn atomic-like orbitals and the bpy MOs can be thought of as mostly electrostatic, increasing in strength with increasing negative charge on bpy.

The NBO analysis shows that complexes **1**−**3** also exhibit a so-called lone vacant non-Lewis-type orbitals on the Zn(II) ion with natural occupations of only ∼0.165 electrons. Although no Zn−N bonds are found within the NBO analysis, this Zn σ^* orbital, possessing the zinc 4s character, highlights the weak Zn−N interactions and σ-accepting character of the Zn center.[44]

The bonding regime across the bpy fragments of **1**−**3** can be deduced from the NBO analysis by the observation of the position of π/π^*-bonding interactions between donor−acceptor atom pairs (Figure 4). The NBO analysis shows that in all three complexes, the more electronegative N3 and N4 atoms of the bpy ligand possess a polarized σ-bonding orbital with the adjacent C30 and C39 atoms, respectively, which are composed of ∼60% N character. However, unlike in **1**, there is no accompanying π-bonding orbital to the N3−C30 and N2−C39 σ bonds. In the cationic species **1**, this degree of polarization is calculated for the N3−C30/N4−C31 σ-bonding NBO as well as for the corresponding π-bonding NBO. As shown in Figures 1 and 4c, the π interactions on the bpy fragment vary across the redox series. According to the NBO analysis: cation **1** exhibits typical aromatic delocalization, with the N3 and N4 atoms forming π interactions with the C30 and C39 atoms, respectively. However, for **2** and **3**, these nitrogens are not involved in any π interactions with the adjacent carbons, but rather the ring-linking C34 and C35 atoms form a π bond. This is symptomatic of the dearomatization of the bpy as a result of sequential one-electron reductions and is in strong agreement with both the present structural data and previous studies in other transition metal complexes of bpy.[22,24,25,45] Our observations are also in line with the investigations into first-row transition metal complexes of bpy made by Wieghardt and co-workers[22,24,43] as well as the subsequent analysis of a series of heteroleptic first-row transition metal complexes of bpy by Irwin et al.[25]

It is clear that increasing the negative charge on bpy is significantly strong enough to modulate the Zn−N bond lengths via increased covalent interaction in the dative coordination bonds. Additionally, secondary effects, such as acute geometric distortions in the bite angle of the β-diketiminate co-ligand, are thought to act constructively; decreasing the energy of the LUMO, and thus increasing the Lewis acidity of the Zn(II) center. Constraining either the Zn−N_{bpy} bond lengths or the β-diketiminate N−Zn−N angles in **1** showed that the energy of the LUMO can be modulated by as much as ∼495 or 615 cm^{-1} by increasing these bond lengths or angles from 1.96 to 2.04 Å and 90 to 100°, respectively (Figures S43 and S44). The more stable 90° N−Zn−N of the β-diketiminate ligand was also accompanied by longer Zn−N bond lengths, which is what is observed in the crystal structure. Thus, these synergistic effects combine to decrease Zn−bpy bond lengths, meaning that the changes in the bond metrics pertaining to the bpy ligand are diagnostic of a purely bpy-centered reduction that results in dearomatization. This is both observed in the crystallography and accurately captured by the NBO analysis, which identifies the loss of C−N π bonds and decreasing C34−C35 bond length in the singly and doubly reduced bpy complexes **2** and **3**. Overall, the bonding between the Zn and bpy moieties consists primarily of electrostatic interactions between positively charged Zn(II) ions and the in-plane nitrogen sp^2 lone pairs of the bpy.

CONCLUSION

In summary, three β-diketiminate-supported zinc complexes of 2,2′-bipyridine were synthesized, in which the oxidation state of the 2,2′-bipyridine moiety is varied from 0 to −2. This provides a homologous series of examples to view the redox behavior of noninnocent 2,2′-bipyridine ligands and how this is manifested by the overall structural and spectroscopic properties of the complex. The bond distances and angles correlate with the charge of the bpy ligand in a linear fashion, providing an insight into the mechanism of interaction between the zinc(II) center and ligand. Theoretical calculations echo the experimental results and demonstrate that the

https://doi.org/10.1021/acsomega.1c02201
ACS Omega 2021, 6, 18325−18332

gain and loss of electrons are localized to the bpy ligand, while the LZn moiety assumes the role of a spectator and Lewis acid.

EXPERIMENTAL SECTION

General Procedures. All manipulations were carried out under an atmosphere of dry argon or nitrogen using the Schlenk line and glovebox techniques. Toluene and *n*-hexane were dried using a Braun solvent drying system and degassed prior to use. Fluorobenzene was dried over CaH_2. Deuterated benzene and THF were dried by refluxing over sodium/potassium under an argon atmosphere prior to use, while deuterated dichloromethane was dried over CaH_2. ^{1}H, ^{13}C, ^{19}F, and ^{11}B NMR spectra were recorded on Bruker Avance II 400 and 600 MHz spectrometers. Elemental analyses were performed at the *Elementaranalyse Labor* of the University of Duisburg-Essen. UV−vis spectra were collected on a Shimadzu UV-2600i UV−vis spectrophotometer. IR spectra were recorded using a Bruker ALPHA-T FTIR spectrometer equipped with a single-reflection ATR sampling module. Commercial reagents were purchased from Aldrich, Acros, or Alfa-Aesar Chemical Co. and used as received. $NaB(C_6F_5)_4$[46] was prepared according to the literature, and LZnI (L = $HC[C(Me)N(Ar)]_2$, Ar = 2,6-*i*$Pr_2C_6H_3$)[47] was prepared in a modified synthetic procedure.

CW X-band (~9.5 GHz) EPR spectra of **2** and **2-d_8** and **3** were collected on a Magnetech 5000 EPR spectrometer at room temperature. Samples were prepared under an argon atmosphere in a glovebox and sealed in glass capillary sample tubes (50 μL) using Hirschmann sealing wax purchased from Fisher Scientific. The room-temperature CW X-band spectrum of **2** was collected with 100 kHz field modulation at 0.1 G amplitude and a 240 s sweep time for four repeat scans. For **2-d_8**, the experimental parameters were kept constant, except for an increase to 0.5 G amplitude and the use of five repeat scans. For the qualitative and quantitative analyses of **2** and **3** in toluene, THF, or CH_2Cl_2 solutions, the samples were prepared at 1 mM concentration and the spectra were collected using 100 KHz field modulation at 0.5 G amplitude and a 60 s sweep time. A digital RC filter was applied with an effective time constant of 0.05 s. All EPR data were processed and analyzed in Matlab 2019b and simulated using the EasySpin package (v. 6.0).[48] Simulation parameters are given in figure captions.

Synthesis of LZnI. An equimolar mixture of LLi and ZnI_2 was suspended in *n*-hexane at −20 °C and stirred for 24 h. The resulting suspension was filtered, and the filtrate was concentrated in vacuo and stored at −30 °C, yielding colorless crystals after 24 h. Yield: 90%. ^{1}H NMR (400 MHz, C_6D_6) δ = 1.18 (d, $^{3}J_{HH}$ = 8.0 Hz, 12H, CH*Me*$_2$), 1.41 (d, $^{3}J_{HH}$ = 8.0 Hz, 12H, CH*Me*$_2$), 1.72 (s, 6H, C*Me*), 3.15 (sept, $^{3}J_{HH}$ = 8.0 Hz, 4H, C*H*Me$_2$), 5.04 (s, 1H, C*H*), 7.15−7.21 (m, 6H, C_6H_3).

Synthesis of **1**. LZnI (250 mg, 0.41 mmol), 2,2′-bipyridine (64 mg, 0.41 mmol), and $Na[B(C_6F_5)_4]$ (288 mg, 0.41 mmol) were suspended in *n*-hexane (40 mL) at ambient temperature and stirred for 12 h. The resulting light-yellow suspension was filtered and the filtrate reduced in vacuo to yield a light-yellow solid. Yield: 480 mg (88.8%). Colorless crystals were obtained by layering *n*-hexane on top of a solution of **1** in fluorobenzene. Melting point: 204 °C (dec). Anal. calcd (%) for $C_{63}H_{49}ZnN_4BF_{20}$ (Mr = 1318.27): C, 57.4; H, 3.75; N, 4.25. Found: C, 56.3; H, 3.53; N, 4.22. ^{1}H NMR (600 MHz, CD_2Cl_2): δ = 0.72 (d, $^{3}J_{HH}$ = 6.0 Hz, 12H, CH*Me*$_2$), 1.18 (d, $^{3}J_{HH}$ = 6.0 Hz, 12H, CH*Me*$_2$), 1.85 (s, 6H, C*Me*), 3.11 (sept, $^{3}J_{HH}$ = 6.0 Hz, 4H, C*H*Me$_2$), 5.15 (s, 1H, C*H*), 7.00−7.16 (m, 6H, C_6H_3), 7.78 (sept, $^{3}J_{HH}$ = 6.0 Hz, 4H, *H*-bpy), 8.22 (d, $^{3}J_{HH}$ = 4.2 Hz, 2H, *H*-bpy), 8.61 (d, $^{3}J_{HH}$ = 4.2 Hz, 2H, *H*-bpy). $^{13}C\{^{1}H\}$ NMR (150 MHz, CD_2Cl_2): δ = 24.2, 24.4, 24.5, 29.0, 96.0 (γ-*C*H), 123.4, 124.5, 126.8, 128.8, 142.4, 143.0, 143.6, 149.5, 149.6, 171.7 (*C*N). ^{19}F NMR (565 MHz, CD_2Cl_2): δ = −133.5(m, 8F, *o-F*), −163.3 (t, $^{3}J_{FF}$ = 22.6 Hz, 4F, *p-F*), −167.3 (m, 8F, *m-F*). ^{11}B NMR (192 MHz, CD_2Cl_2): δ = −16.6. ^{1}H NMR (600 MHz, d_8-THF): δ = 0.76 (d, $^{3}J_{HH}$ = 6.0 Hz, 12H, CH*Me*$_2$), 1.20 (d, $^{3}J_{HH}$ = 6.0 Hz, 12H, CH*Me*$_2$), 1.87 (s, 6H, C*Me*), 3.20 (sept, $^{3}J_{HH}$ = 6.0 Hz, 4H, C*H*Me$_2$), 5.23 (s, 1H, C*H*), 7.03−7.05 (m, 6H, C_6H_3), 7.92 (sext, $^{3}J_{HH}$ = 6.0 Hz, 2H, *H*-bpy), 8.35 (sext, $^{3}J_{HH}$ = 6.0 Hz, 2H, *H*-bpy), 8.56 (d, $^{3}J_{HH}$ = 4.2 Hz, 2H, *H*-bpy), 8.72 (d, $^{3}J_{HH}$ = 4.2 Hz, 2H, *H*-bpy). $^{13}C\{^{1}H\}$ NMR (150 MHz, d_8-THF): δ = 24.1, 24.5, 24.6, 29.3, 96.2 (γ-*C*H), 124.5, 124.8, 127.2, 129.4, 142.8, 143.6, 144.3, 150.2, 150.4, 171.8 (*C*N). ATR-IR: ν 2965, 1643, 1513, 1459, 1385, 1313, 1267, 1086, 1027, 975, 803, 766, 755, 682, 660 cm^{-1}.

From **2** *to* **1**. Equimolar amounts of **2** and $[Ph_3C][B(C_6F_5)_4]$ were dissolved at ambient temperature in CD_2Cl_2 in an NMR tube, resulting in an immediate color change to yellow. An in situ ^{1}H NMR spectrum showed the quantitative formation of **1**.

From **3** *to* **1**. A 1:2 molar ratio of **3** and $[Ph_3C][B(C_6F_5)_4]$ were dissolved in THF-d_8 at ambient temperature in an NMR tube, resulting in an immediate color change to yellow. An in situ ^{1}H NMR spectrum showed the quantitative formation of **1**.

Synthesis of **2** *and* **2-d_8**. LZnI (610 mg, 1 mmol), 2,2′-bipyridine (156 mg, 1 mmol), and KC_8 (135 mg, 1 mmol) were suspended in toluene (50 mL) at ambient temperature and stirred for 12 h. The suspension was filtered, and the resulting black filtrate concentrated to 5 mL and stored at 4 °C. Dark black crystals were formed within 24 h. Yield: 250 mg (38.8%). Melting point: 200 °C (dec). Anal. calcd (%) for $C_{39}H_{49}ZnN_4$ (Mr = 639.23): C, 73.3; H, 7.73; N, 8.76. Found: C, 73.2; H, 7.84; N, 8.60. ATR-IR: ν 2958, 2922, 2868, 1544, 1512, 1489, 1456, 1436, 1398, 1312, 1292, 1269, 1177, 1095, 1006, 959, 936, 853, 792, 758, 715, 656, 455, 413 cm^{-1}. The deuterated analog **2-d_8** was prepared in a similar method using bpy-d_8 as the precursor.

Synthesis of **3**. THF (30 mL) was added to a mixture of LZnI (150 mg, 0.25 mmol), 2,2′-bipyridine (38 mg, 0.25 mmol), [2.2.2]cryptand (92 mg, 0.25 mmol), and KC_8 (66 mg, 0.5 mmol) at −78 °C, and the resulting suspension was warmed to ambient temperature within 12 h. The solvent was removed in a vacuum, and the resulting residue was extracted with toluene (40 mL). The filtrate was concentrated to 5 mL and stored at 4 °C. Dark orange crystals formed within 24 h. Yield: 105 mg (40.5%). Melting point: 207 °C (dec). Anal. calcd (%) for $C_{57}H_{85}ZnN_6O_6K$ (Mr = 1054.82): C, 64.9; H, 8.12; N, 7.97. Found: C, 64.7; H, 8.32; N, 7.50. ^{1}H NMR (600 MHz, d_8-THF): δ = 1.16 (d, $^{3}J_{HH}$ = 6.0 Hz, 12H, CH*Me*$_2$), 1.37 (d, $^{3}J_{HH}$ = 6.0 Hz, 12H, CH*Me*$_2$), 1.56 (s, 6H, C*Me*), 2.31 (s, 3H, toluene), 2.52 (m, 12H, crypt-CH_2), 3.47 (m, 4H, C*H*Me$_2$), 3.51 (m, 12H, crypt-CH_2), 3.55 (s, 12H, crypt-CH_2), 4.48 (s, 1H, C*H*), 6.96−7.20 (m, 11H, C_6H_3, toluene). $^{13}C\{^{1}H\}$ NMR (150 MHz, d_8-THF): δ = 21.5, 25.7, 25.8, 54.9, 68.5, 71.4, 123.5, 124.5, 126.1, 128.9, 129.7, 138.5, 143.7 (*C*N). ^{1}H NMR (400 MHz, CD_2Cl_2): δ = 1.13 (d, $^{3}J_{HH}$ = 8.0 Hz, 12H, CH*Me*$_2$), 1.24 (d, $^{3}J_{HH}$ = 6.0 Hz, 12H, CH*Me*$_2$), 1.62

https://doi.org/10.1021/acsomega.1c02201
ACS Omega 2021, 6, 18325−18332

(s, 6H, C*Me*), 2.34 (s, 3H, toluene), 2.53, 3.51, 3.58 (m, crypt-CH_2), 3.54 (m, 4H, $CHMe_2$), 4.67 (s, 1H, C*H*), 7.10−7.34 (m, 16H, C_6H_3, toluene, *H*-bpy), 7.82 (sext, $^3J_{HH}$ = 8.0 Hz, 1H, *H*-bpy), 8.43 (d, $^3J_{HH}$ = 4.2 Hz, 1H, *H*-bpy), 8.65 (d, $^3J_{HH}$ = 4.2 Hz, 1H, *H*-bpy). $^{13}C\{^1H\}$ NMR (150 MHz, CD_2Cl_2): δ = 21.7, 24.2, 24.9, 25.9, 28.1, 68.1, 71.0, 93.0, 121.3, 123.6, 124.3, 124.5, 125.8, 128.7, 129.5, 137.4, 138.5, 144.1, 146.5, 149.7, 156.6, 166.6. ATR-IR: ν 1854, 2863, 2809, 1516, 1456, 1434, 1406, 1352, 1317, 1281, 1258, 1176, 1098, 1077, 963, 950, 924, 788, 756, 725, 672, 621, 521, 396 cm^{-1}.

*From **2** to **3***. A 1:1:1 molar mixture of compound **2**, KC_8, and [2.2.2]cryptand were suspended in an NMR tube in THF-d_8 at ambient temperature, resulting in an immediate color change to dark green. An in situ ^1H NMR spectrum showed the quantitative formation of **3**.

■ ASSOCIATED CONTENT

Supporting Information

The Supporting Information is available free of charge at https://pubs.acs.org/doi/10.1021/acsomega.1c02201.

Detailed synthetic procedures and analytical data, NMR, IR, EPR, and UV−vis spectra, and computational details (PDF)

CCDC-2062506 (**1**), CCDC-2062507 (**2**), CCDC-2062508 (**3**), and CCDC-2067984 (**3#**) contain the supplementary crystallographic data (CIF)

■ AUTHOR INFORMATION

Corresponding Authors

George E. Cutsail III − *Institute for Inorganic Chemistry, University of Duisburg-Essen, 45117 Essen, Germany; Max Planck Institute for Chemical Energy Conversion (CEC), 45470 Mülheim an der Ruhr, Germany;* orcid.org/0000-0002-7378-9474; Email: george.cutsail@cec.mpg.de

Stephan Schulz − *Institute for Inorganic Chemistry and Center for Nanointegration Duisburg-Essen (CENIDE), University of Duisburg-Essen, 45117 Essen, Germany;* orcid.org/0000-0003-2896-4488; Email: stephan.schulz@uni-due.de

Authors

Bin Li − *Institute for Inorganic Chemistry, University of Duisburg-Essen, 45117 Essen, Germany;* orcid.org/0000-0002-8029-8841

Blaise L. Geoghegan − *Institute for Inorganic Chemistry, University of Duisburg-Essen, 45117 Essen, Germany; Max Planck Institute for Chemical Energy Conversion (CEC), 45470 Mülheim an der Ruhr, Germany;* orcid.org/0000-0001-9543-102X

Christoph Wölper − *Institute for Inorganic Chemistry, University of Duisburg-Essen, 45117 Essen, Germany*

Complete contact information is available at: https://pubs.acs.org/10.1021/acsomega.1c02201

Author Contributions

The manuscript was written through the contributions of all authors. All authors have given approval to the final version of the manuscript.

Notes

The authors declare no competing financial interest.

■ ACKNOWLEDGMENTS

The authors thank Julia Haak for assistance of EPR data acquisition. They are also thankful to the Max-Planck-Gesellschaft (GEC) and the University of Duisburg-Essen (StS) for their generous financial support.

■ REFERENCES

(1) Constable, E. C. Homoleptic Complexes of 2,2′-Bipyridine. In *Advances in Inorganic Chemistry*; Sykes, A. G., Ed.; Vol. *34*; Academic Press: San Diego, CA, 1989; pp 1−63.

(2) Constable, E. C.; Housecroft, C. E. The Early Years of 2,2′-Bipyridine—A Ligand in Its Own Lifetime. *Molecules* **2019**, *24*, No. 3951.

(3) Smith, A. P.; Fraser, C. L. Bipyridine Ligands. In *Comprehensive Coordination Chemistry II*; McCleverty, J. A., Meyer, T. J., Eds.; Pergamon: Oxford, 2003; pp 1−23.

(4) Schubert, U. S.; Eschbaumer, C. Macromolecules Containing Bipyridine and Terpyridine Metal Complexes: Towards Metallosupramolecular Polymers. *Angew. Chem., Int. Ed.* **2002**, *41*, 2892−2926.

(5) Ye, B.-H.; Tong, M.-L.; Chen, X.-M. Metal-Organic Molecular Architectures with 2,2′-Bipyridyl-Like and Carboxylate Ligands. *Coord. Chem. Rev.* **2005**, *249*, 545−565.

(6) Wu, Y.; Lu, L.; Feng, J.; Li, Y.; Sun, Y.; Ma, A. Design and Construction of Diverse Structures of Coordination Polymers: Photocatalytic Properties. *J. Solid State Chem.* **2017**, *245*, 213−218.

(7) Malkov, A. V.; Kocovsky, P. Chiral Bipyridine Derivatives in Asymmetric Catalysis. *Curr. Org. Chem.* **2003**, *7*, 1737−1757.

(8) Grice, K. A.; Kubiak, C. P. Recent Studies of Rhenium and Manganese Bipyridine Carbonyl Catalysts for the Electronchemical Reduction of CO_2. In *Advances in Inorganic Chemistry*; Aresta, M., Van Eldik, R., Eds., Vol. *66*; Academic Press: New York, 2014, pp 163−188.

(9) Fukuzumi, S.; Jung, J.; Yamada, Y.; Kojima, T.; Nam, W. Homogeneous and Heterogeneous Photocatalytic Water Oxidation by Persulfate. *Chem. Asian J.* **2016**, *11*, 1138−1150.

(10) Barbieri, A.; Ventura, B.; Ziessel, R. Photoinduced Energy-Transfer Dynamics in Multichromophoric Arrays Containing Transition Metal Complexes and Organic Modules. *Coord. Chem. Rev.* **2012**, *256*, 1732−1741.

(11) Happ, B.; Winter, A.; Hager, M. D.; Schubert, U. S. Photogenerated Avenues in Macromolecules Containing Re(I), Ru(II), Os(II), and Ir(III) Metal Complexes of Pyridine-Based Ligands. *Chem. Soc. Rev.* **2012**, *41*, 2222−2255.

(12) Nikiforov, G. B.; Roesky, H. W.; Noltemeyer, M.; Schmidt, H.-G. Reactivity of $Ti(bipy)_3$ and Preparation of the $Li(THF)_4[Al(bipy)_2]$ Complex with the Dinegative Bipy Ligand. *Polyhedron* **2004**, *23*, 561−566.

(13) Mansell, S. M.; Norman, N. C.; Russell, C. A. Boron−Nitrogen Analogues of the Fluorenyl Anion. *Dalton Trans.* **2010**, *39*, 5084−5086.

(14) Mansell, S. M.; Adams, C. J.; Bramham, G.; Haddow, M. F.; Kaim, W.; Norman, N. C.; McGrady, J. E.; Russell, C. A.; Udeen, S. J. Synthesis and Characterisation of the Persistent Radical $[BCl_2(bipy)]$. *Chem. Commun.* **2010**, *46*, 5070−5072.

(15) Liu, S.; Légaré, M.-A.; Seufert, J.; Prieschl, D.; Rempel, A.; Englert, L.; Dellermann, T.; Paprocki, V.; Stoy, A.; Braunschweig, H. 2,2′-Bipyridyl as a Redox-Active Borylene Abstraction Agent. *Inorg. Chem.* **2020**, *59*, 10866−10873.

(16) Gore-Randall, E.; Irwin, M.; Denning, M. S.; Goicoechea, J. M. Synthesis and Characterization of Alkali-Metal Salts of 2,2′- and 2,4′-Bipyridyl Radicals and Dianions. *Inorg. Chem.* **2009**, *48*, 8304−8316.

(17) Bock, H.; Lehn, J.-M.; Pauls, J.; Holl, S.; Krenzel, V. Sodium Salts of the Bipyridine Dianion: Polymer $[(bpy)^{2-}\{Na^+(dme)\}_2]_\infty$, Cluster $[(Na_8O)^{6+}Na^+_6(bpy)_6{}^{2-}(tmeda)_6]$, and Monomer $[(bpy)^{2-}\{Na^+(pmdta)\}_2]$. *Angew. Chem., Int. Ed.* **1999**, *38*, 952−955.

(18) Gray, P. A.; Krause, K. D.; Burford, N.; Patrick, B. O. Cationic 2,2′-Bipyridine Complexes of Germanium(II) and Tin(II). *Dalton Trans.* **2017**, *46*, 8363−8366.
(19) Booth, C. H.; Walter, M. D.; Kazhdan, D.; Hu, Y.-J.; Lukens, W. W.; Bauer, E. D.; Maron, L.; Eisenstein, O.; Andersen, R. A. Decamethylytterbocene Complexes of Bipyridines and Diazabutadienes: Multiconfigurational Ground States and Open-Shell Singlet Formation. *J. Am. Chem. Soc.* **2009**, *131*, 6480−6491.
(20) Roitershtein, D.; Domingos, Â.; Pereira, L. C. J.; Ascenso, J. R.; Marques, N. Coordination of 2,2′-Bipyridyl and 1,10-Phenanthroline to Yttrium and Lanthanum Complexes Based on a Scorpionate Ligand. *Inorg. Chem.* **2003**, *42*, 7666−7673.
(21) Bowman, A. C.; England, J.; Sproules, S.; Weyhermüller, T.; Wieghardt, K. Electronic Structures of Homoleptic [Tris(2,2)′-bipyridine)M]^n Complexes of the Early Transition Metals (M = Sc, Y, Ti, Zr, Hf, V, Nb, Ta; n = 1+, 0, 1−, 2−, 3−): An Experimental and Density Functional Theoretical Study. *Inorg. Chem.* **2013**, *52*, 2242−2256.
(22) Scarborough, C. C.; Wieghardt, K. Electronic Structure of 2,2′-Bipyridine Organotransition-Metal Complexes. Establishing the Ligand Oxidation Level by Density Functional Theoretical Calculations. *Inorg. Chem.* **2011**, *50*, 9773−9793.
(23) Wang, M.; England, J.; Weyhermüller, T.; Wieghardt, K. Molecular and Electronic Structures of the Members of the Electron Transfer Series $[Mn(bpy)_3]^n$ (n = 2+, 1+, 0, 1−) and $[Mn(tpy)_2]^m$ (m = 4+, 3+, 2+, 1+, 0). An Experimental and Density Functional Theory Study. *Inorg. Chem.* **2014**, *53*, 2276−2287.
(24) Scarborough, C. C.; Sproules, S.; Weyhermüller, T.; DeBeer, S.; Wieghardt, K. Electronic and Molecular Structures of the Members of the Electron Transfer Series $[Cr(tbpy)_3]^n$ (n = 3+, 2+, 1+, 0): An X-ray Absorption Spectroscopic and Density Functional Theoretical Study. *Inorg. Chem.* **2011**, *50*, 12446−12462.
(25) Irwin, M.; Doyle, L. R.; Krämer, T.; Herchel, R.; McGrady, J. E.; Goicoechea, J. M. A Homologous Series of First-Row Transition-Metal Complexes of 2,2′-Bipyridine and their Ligand Radical Derivatives: Trends in Structure, Magnetism, and Bonding. *Inorg. Chem.* **2012**, *51*, 12301−12312.
(26) Irwin, M.; Jenkins, R. K.; Denning, M. S.; Krämer, T.; Grandjean, F.; Long, G. J.; Herchel, R.; McGrady, J. E.; Goicoechea, J. M. Experimental and Computational Study of the Structural and Electronic Properties of Fe^{II}(2,2′-bipyridine)$(mes)_2$ and $[Fe^{II}$(2,2′-bipyridine)$(mes)_2]^-$, a Complex Containing a 2,2′-Bipyridyl Radical Anion. *Inorg. Chem.* **2010**, *49*, 6160−6171.
(27) Katari, M.; Carmichael, D.; Jacquemin, D.; Frison, G. Structure of Electronically Reduced N-Donor Bidentate Ligands and Their Heteroleptic Four-Coordinate Zinc Complexes: A Survey of Density Functional Theory Results. *Inorg. Chem.* **2019**, *58*, 7169−7179.
(28) Tsai, Y.-C. The Chemistry of Univalent Metal β-Diketiminates. *Coord. Chem. Rev.* **2012**, *256*, 722−758.
(29) Webster, R. L. β-Diketiminate Complexes of the First Row Transition Metals: Applications in Catalysis. *Dalton Trans.* **2017**, *46*, 4483−4498.
(30) Khusniyarov, M. M.; Bill, E.; Weyhermüller, T.; Bothe, E.; Wieghardt, K. Hidden Noninnocence: Theoretical and Experimental Evidence for Redox Activity of a β-Diketiminate(1−) Ligand. *Angew. Chem., Int. Ed.* **2011**, *50*, 1652−1655.
(31) Takaichi, J.; Morimoto, Y.; Ohkubo, K.; Shimokawa, C.; Hojo, T.; Mori, S.; Asahara, H.; Sugimoto, H.; Fujieda, N.; Nishiwaki, N.; Fukuzumi, S.; Itoh, S. Redox Chemistry of Nickel(II) Complexes Supported by a Series of Noninnocent β-Diketiminate Ligands. *Inorg. Chem.* **2014**, *53*, 6159−6169.
(32) Marshak, M. P.; Chambers, M. B.; Nocera, D. G. Cobalt in a Bis-β-diketiminate Environment. *Inorg. Chem.* **2012**, *51*, 11190−11197.
(33) Ibrahim, S. K.; Khvostov, A. V.; Lappert, M. F.; Maron, L.; Perrin, L.; Pickett, C. J.; Protchenko, A. V. An Electrochemical and DFT Study on Selected β-Diketiminato Metal Complexes. *Dalton Trans.* **2006**, 2591−2596.
(34) Köhler, F. H. Paramagnetic Complexes in Solution: The NMR Approach. In *eMagRes*; Harris, R. K., Wasylishen, R. L., Eds.; John Wiley & Sons, Ltd, 2011.
(35) Evans, D. F. 400. The determination of the paramagnetic susceptibility of substances in solution by nuclear magnetic resonance. *J. Chem. Soc.* **1959**, 2003−2005.
(36) Boersma, J.; Mackor, A.; Noltes, J. G. ESR Study of Monoalkylzinc-2,2′-Bipyridine Complexes RZn·Bipy. *J. Organomet. Chem.* **1975**, *99*, 337−341.
(37) Creutz, C. Bipyridine Radical Ions. *Comments Inorg. Chem.* **1982**, *1*, 293−311.
(38) Víchová, J.; Hartl, F.; Vlček, A. Wavelength-Dependent Photosubstitution and Excited-State Dynamics of $[Cr(CO)_4$(2,2′-bipyridine)]: A Quantum Yield and Picosecond Absorption Study. *J. Am. Chem. Soc.* **1992**, *114*, 10903−10910.
(39) Mirabi, B.; Poh, W. C.; Armstrong, D.; Lough, A. J.; Fekl, U. Why Diorganyl Zinc Lewis Acidity Dramatically Increases with Narrowing C−Zn−C Bond Angle. *Inorg. Chem.* **2020**, *59*, 2621−2625.
(40) Foster, J. P.; Weinhold, F. Natural Hybrid Orbitals. *J. Am. Chem. Soc.* **1980**, *102*, 7211−7218.
(41) Reed, A. E.; Weinstock, R. B.; Weinhold, F. Natural Population Analysis. *J. Chem. Phys.* **1985**, *83*, 735−746.
(42) Dhara, A. K.; Singh, U. P.; Ghosh, K. Radical Pathways and O_2 Participation in Benzyl Alcohol Oxidation, and Catechol and o-Aminophenol Oxidase Activity Studies with Novel Zinc Complexes: An Experimental and Theoretical Investigation. *Inorg. Chem. Front.* **2016**, *3*, 1543−1558.
(43) Flores, J. A.; Andino, J. G.; Lord, R. L.; Wolfe, R. J.; Park, H.; Pink, M.; Telser, J.; Caulton, K. G. Probing Redox Noninnocence of Copper and Zinc Bis-pyridylpyrrolides. *Eur. J. Inorg. Chem.* **2018**, *2018*, 4893−4904.
(44) Usman, M.; Khan, R. A.; Alsalme, A.; Alharbi, W.; Alharbi, K. H.; Jaafar, M. H.; Abu Khanjer, M.; Tabassum, S. Structural, Spectroscopic, and Chemical Bonding Analysis of Zn(II) Complex [Zn(sal)](H_2O): Combined Experimental and Theoretical (NBO, QTAIM, and ELF) Investigation. *Crystals* **2020**, *10*, No. 259.
(45) Bowman, A. C.; Sproules, S.; Wieghardt, K. Electronic Structures of the $[V(^tbpy)_3]^z$ (z = 3+, 2+, 0, 1−) Electron Transfer Series. *Inorg. Chem.* **2012**, *51*, 3707−3717.
(46) Forster, F.; Metsänen, T. T.; Irran, E.; Hrobárik, P.; Oestreich, M. Cooperative Al−H Bond Activation in DIBAL-H: Catalytic Generation of an Alumenium-Ion-Like Lewis Acid for Hydrodefluorinative Friedel−Crafts Alkylation. *J. Am. Chem. Soc.* **2017**, *139*, 16334−16342.
(47) Prust, J.; Most, K.; Müller, I.; Stasch, A.; Roesky, H. W.; Uson, I. Synthesis and Structures of Vinamidine Mn^{II}, Zn^{II}, and Cd^{II} Iodine Derivatives. *Eur. J. Inorg. Chem.* **2001**, 1613−1616.
(48) Stoll, S.; Schweiger, A. EasySpin, a comprehensive software package for spectral simulation and analysis in EPR. *J. Magn. Reson.* **2006**, *178*, 42−55.

https://doi.org/10.1021/acsomega.1c02201
ACS Omega 2021, 6, 18325−18332